

Study on fluid-structure interaction in liquid oxygen feeding pipe systems using finite volume method

Xin Wei · Bing Sun

Received: 1 April 2010 / Revised: 13 August 2010 / Accepted: 16 December 2010
©The Chinese Society of Theoretical and Applied Mechanics and Springer-Verlag Berlin Heidelberg 2011

Abstract The fluid-structure interaction may occur in space launch vehicles, which would lead to bad performance of vehicles, damage equipments on vehicles, or even affect astronauts' health. In this paper, analysis on dynamic behavior of liquid oxygen (LOX) feeding pipe system in a large scale launch vehicle is performed, with the effect of fluid-structure interaction (FSI) taken into consideration. The pipe system is simplified as a planar FSI model with Poisson coupling and junction coupling. Numerical tests on pipes between the tank and the pump are solved by the finite volume method. Results show that restrictions weaken the interaction between axial and lateral vibrations. The reasonable results regarding frequencies and modes indicate that the FSI affects substantially the dynamic analysis, and thus highlight the usefulness of the proposed model. This study would provide a reference to the pipe test, as well as facilitate further studies on oscillation suppression.

Keywords Fluid-structure interaction · Liquid oxygen · Finite volume method

Nomenclature

- A cross-sectional area
 E Young modulus of elasticity

e	pipe wall thickness
I	second moment of cross-sectional area
K	liquid bulk modulus
L	length
M	bending moment
m	mass
P	pressure (cross-sectional average)
Q	lateral shear force
R	(inner pipe) radius
t	time
u	pipe displacement
\dot{u}	pipe velocity
V	fluid velocity (cross-sectional average)
x	lateral coordinate (out-of-plane, vertical)
y	lateral coordinate (in-plane, horizontal)
z	axial coordinate (distance along pipe)
Δt	time step (numerical grid length on t -axis)
Δz	element length (numerical grid length on z -axis)
$\dot{\theta}$	rotational velocity of pipe
ν	Poisson ratio
ρ	mass density
σ	normal stress

Subscripts

f	fluid
t	pipe
x	lateral direction (out-of-plane, vertical)
y	lateral direction (in-plane, horizontal)
z	axial direction
0	initial value

Superscripts

n	number of node
*	modified value

1 Introduction

In flights of large scale launch vehicles with liquid rocket engines, axial coupled vibrations have always been observed [1,2]. The vibrations arise when the frequency of

X. Wei (✉)
Institute of Telecommunication Satellite,
China Academy of Space Technology,
100194 Beijing, China
e-mail: buaa_weixin@126.com

B. Sun
School of Astronautics,
Beihang University, 100191 Beijing, China

pressure oscillation in the propulsion system closely matches that of the vehicle structure. As the structure is difficult to change after design, usually our interest would focus on the propulsion system which includes feeding pipes and engines.

As an important part of propulsion system study, the dynamic character of feeding pipe system is proposed as one of the key points for the analysis with the fluid-structure interaction (FSI) taken into consideration. Although the effect of FSI in liquid-filled pipes has been researched broadly [3,4], it is necessary for large scale launch vehicles design and manufacture to reinforce theoretical research on the FSI dynamic behavior of the feeding pipe systems.

Skalak [5] proposed the FSI theory as an extension of the conventional waterhammer theory. Wiggert et al. [6] built an FSI model to consider Poisson coupling and junction coupling, which made an advancement for the FSI theory. Poisson coupling relates pressures in the liquid to axial stresses in the pipes through the radial vibrations of the pipe walls. Friction coupling is the mutual friction between the liquid and the axially vibrating pipe wall. For solving the model of FSI, the method of characteristics (MOC) was popular [3,6], and was improved later [7]. In addition, Zhang et al. [8] applied the finite element method (FEM) to these problems, Zhang and Gay [9] presented an immersed finite element method (IFEM) for the solution of FSI problems, and Giesecke [10] solved relevant FSI mechanisms by an MOC-FEM hybrid method. Although successfully applied in the field of fluid dynamic and heat transfer, the finite volume method (FVM) was not used to solve FSI problems. With the clear physics meaning in every term of the integral equations and a well-documented numerical procedure, the FVM guarantees the conservation of the initial differential equations, as well as the conservation of variable in the whole solution domain by keeping characteristic variable conservation in every control volume. Therefore, the FVM is adopted in present paper to solve the FSI problems for LOX feeding pipe systems.

The control equations of the FSI model were solved by the FVM in the time domain under the well-posed condition. Through numerical calculation, the dynamic response of the LOX pipes was studied, and the FSI mechanisms was discussed.

2 Description of mathematical model

As shown in Fig. 1, one liquid-filled pipe element is assumed to be a planar model, which can vibrate in the axial (longitude) and lateral directions, neglecting vibration in the vertical direction. In other words, the fluid-filled pipe system can only move in the y - z plane without consideration of motion in x -direction. The parameters interested include pipe wall axial velocity \dot{u}_z , pipe wall lateral velocity \dot{u}_y , fluid pressure P , fluid velocity V , pipe wall axial stress σ_z , pipe wall lateral shear force Q_y , pipe angular velocity $\dot{\theta}_x$ and bending moment M_x .

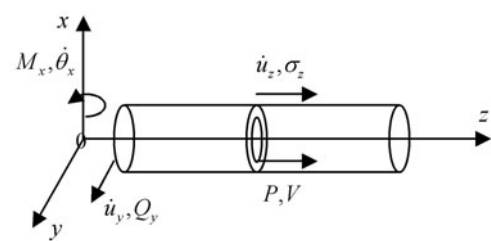


Fig. 1 Element of liquid-filled pipe hint

For simplification, some assumptions are made, including: (1) The fluid is considered as 1D axial flow, with changes in the radial direction neglected; (2) The hoop stress of the pipe wall section is equally distributed; (3) The pipe wall is a linear elastic body.

According to the FSI mechanisms including Poisson coupling and friction coupling, with the Timoshenko beam mechanisms taken into consideration, the motion differential equations were built in the axial and lateral directions for a liquid-filled pipe, as set up by Wiggert [6].

The four axial motion differential equations are written as Eqs. (1)–(4).

The fluid axial motion equation with the viscosity taken into consideration is

$$\frac{\partial V}{\partial t} + \frac{1}{\rho_f} \frac{\partial P}{\partial z} + R_f V = 0, \quad (1)$$

where ρ_f is fluid density, R_f is fluid viscosity damp coefficient, t is time, z is distance of z -direction.

The fluid continuity equation with the compressibility taken into consideration is

$$\frac{\partial V}{\partial z} + \frac{1}{K^*} \frac{\partial P}{\partial t} - 2\nu \frac{\partial \dot{u}_z}{\partial z} = 0, \quad (2)$$

where ν is Poisson ratio, K^* is fluid bulk modulus correction.

The pipe axial motion equation is

$$\frac{\partial \dot{u}_z}{\partial t} - \frac{1}{\rho_t} \frac{\partial \sigma_z}{\partial z} - R_t V = 0, \quad (3)$$

where ρ_t is density of pipe wall, R_t is pipe damp coefficient.

The pipe stress-strain relation with the fluid pressure effect taken into consideration is

$$\frac{\partial \dot{u}_z}{\partial z} - \frac{1}{E} \frac{\partial \sigma_z}{\partial t} = -\frac{\nu R}{Ee} \frac{\partial P}{\partial t}, \quad (4)$$

where E is Young modulus, R is inner radius, e is wall thickness.

The lateral motion differential equations are also written as

$$\frac{\partial \dot{u}_y}{\partial t} + \frac{1}{\rho A} \frac{\partial Q_y}{\partial z} = 0, \quad (5)$$

$$\frac{\partial \dot{u}_y}{\partial z} + \frac{1}{GA_t} \frac{\partial Q_y}{\partial t} = -\dot{\theta}_x, \quad (6)$$

where inertia per length $\rho A = \rho_t A_t + \rho_f A_f$, and G is the pipe wall shear modulus.

$$\frac{\partial \theta_x}{\partial t} + \frac{1}{\rho I} \frac{\partial M_x}{\partial z} = \frac{1}{\rho I} Q_y, \quad (7)$$

$$\frac{\partial \theta_x}{\partial z} + \frac{1}{EI_t} \frac{\partial M_x}{\partial t} = 0, \quad (8)$$

where I is second moment of area, equivalent moment of the inertia per length $\rho I = \rho_t I_t + \rho_f I_f$.

3 Numerical solutions by FVM

According to the liquid-filled pipe axial motion differential equations (1)–(4), the axial motion difference equations can be achieved by time discrete integral method in a staggered grid.

Take Eq. (1) as an example, the integral form in the control volume is written as

$$\int_{\Delta t} \int_{\Delta V} \left(\frac{\partial V}{\partial t} + \frac{1}{\rho_f} \frac{\partial P}{\partial z} + R_f V \right) dV dt = 0. \quad (9)$$

The selected control volume is named as control volume V , as shown in Fig. 2.

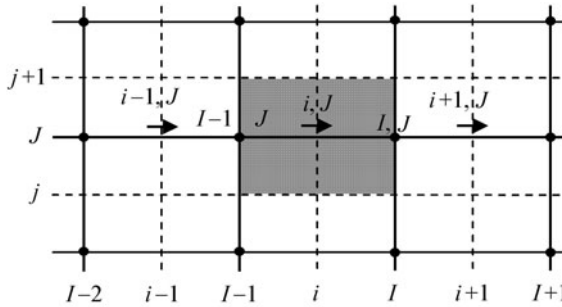


Fig. 2 Control volume V and nodes distribution

The left first integral term in Eq. (9) can be written as

$$\int_{\Delta V} \int_{\Delta t} \frac{\partial V}{\partial t} dV dt = \int_{\Delta V} \frac{V_i^{n+1} - V_i^n}{\Delta t} dV dt = (V_i^{n+1} - V_i^n) \Delta V.$$

For 1D grid, $\Delta V = A_{i,j} \Delta z$, the above equation may be written as

$$\begin{aligned} \int_{\Delta V} \int_{\Delta t} \frac{\partial V}{\partial t} dV dt &= \int_{\Delta V} \frac{V_i^{n+1} - V_i^n}{\Delta t} dV dt \\ &= (V_i^{n+1} - V_i^n) A_{i,j} \Delta z. \end{aligned} \quad (10)$$

In Eq. (10) $A_{i,j}$ is the area of the control volume interface of the grid. For 1D, it is equal to the section area of the fluid flowed in the pipe A_f . Δz is the 1D grid width δz , called as the space step.

In the second integral term in Eq. (9), the value of the left and right interfaces of the control volume are the nodes

value of the P control volume, written as P_I and P_{I-1} .

$$\begin{aligned} \int_{\Delta t} \int_{\Delta V} \frac{1}{\rho_f} \frac{\partial P}{\partial z} dV dt &= \frac{1}{\rho_f} \int_{\Delta t} \frac{P_e - P_w}{\Delta z} A_{I,J} dz dt \\ &= \frac{1}{\rho_f} \int_{\Delta t} \frac{P_I - P_{I-1}}{\Delta z} A_{I,J} dz dt. \end{aligned}$$

Using the method of weighed average and integration we can obtain a relation as

$$\begin{aligned} \int_{\Delta t} \int_{\Delta V} \frac{1}{\rho_f} \frac{\partial P}{\partial z} dV dt &= \frac{A_{I,J} \Delta t}{\rho_f} [\theta(P_I^{n+1} - P_{I-1}^{n+1}) \\ &\quad + (1 - \theta)(P_I^n - P_{I-1}^n)]. \end{aligned} \quad (11)$$

In the third term in Eq. (9), V_i at the node is used instead of the average of the element the node belongs to.

$$\int_{\Delta t} \int_{\Delta V} R_f V dV dt = R_f A_{I,J} \Delta z \Delta t [\theta V_i^{n+1} + (1 - \theta) V_i^n]. \quad (12)$$

Substituting Eqs. (10)–(12) into Eq. (9), the differencing scheme of Eq. (1) can be written as

$$(\rho_f + \rho_f R_f \Delta t \theta) V_i^{n+1} + \frac{\Delta t}{\Delta z} \theta (P_I^{n+1} - P_{I-1}^{n+1}) = f_1(V^n, P^n). \quad (13a)$$

The right side term $f_1(V^n, P^n)$ is a function of the value of one node at the n time layer, which can be written as

$$\begin{aligned} f_1(V^n, P^n) &= [\rho_f + \rho_f R_f \Delta t (\theta - 1)] V_i^n \\ &\quad + \frac{\Delta t}{\Delta z} (1 - \theta) (P_{I-1}^n - P_I^n). \end{aligned} \quad (13b)$$

Equation (2) is treated with the same discrete method, but in control volume P as shown in Fig. 3.

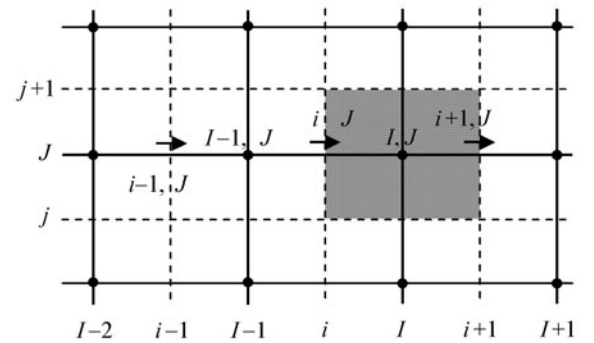


Fig. 3 Control volume P and nodes distribution

According to the basic principle for discretizing the above equations, the axial motion difference equations can be obtained as

$$\begin{aligned}
& (\rho_f + \rho_f R_f \Delta t \theta) V_i^{n+1} + \frac{\Delta t}{\Delta z} \theta (P_I^{n+1} - P_{I-1}^{n+1}) \\
& = f_1(V^n, P^n), \\
& \theta (V_{i+1}^{n+1} - V_i^{n+1}) + \frac{\Delta z}{K^* \Delta t} P_I^{n+1} - 2\nu \theta [(\dot{u}_z)_{i+1}^{n+1} \\
& - (\dot{u}_z)_i^{n+1}] = f_2(V^n, P^n, \dot{u}_z^n), \\
& -\rho_t R_t \Delta z \Delta t \theta V_i^{n+1} + \rho_t \Delta z (\dot{u}_z)_i^{n+1} - \Delta t \theta [(\sigma_z)_I^{n+1} \\
& - (\sigma_z)_{I-1}^{n+1}] = f_3(V^n, \dot{u}_z^n, \sigma_z^n), \\
& \frac{\nu R}{e} A_{I,J} \Delta z P_I^{n+1} + A_{I,J} E \Delta t \theta [(\dot{u}_z)_{i+1}^{n+1} - (\dot{u}_z)_i^{n+1}] \\
& - A_{I,J} \Delta z (\sigma_z)_I^{n+1} = f_4(P^n, \dot{u}_z^n, \sigma_z^n).
\end{aligned} \tag{14a}$$

The related functions at one node at the n time layer can be written as

$$\begin{aligned}
f_1(V^n, P^n) &= [\rho_f + \rho_f R_f \Delta t (\theta - 1)] V_i^n \\
&+ \frac{\Delta t}{\Delta z} (1 - \theta) (P_{I-1}^n - P_I^n), \\
f_2(V^n, P^n, \dot{u}_z^n) &= (\theta - 1) (V_{i+1}^n - V_i^n) + \frac{\Delta z}{K^* \Delta t} P_I^n \\
&+ 2\nu (1 - \theta) [(\dot{u}_z)_{i+1}^n - (\dot{u}_z)_i^n], \\
f_3(V^n, \dot{u}_z^n, \sigma_z^n) &= \rho_t R_t \Delta z \Delta t (1 - \theta) V_i^n + \rho_t \Delta z (\dot{u}_z)_i^n \\
&+ \Delta t (1 - \theta) [(\sigma_z)_I^n - (\sigma_z)_{I-1}^n], \\
f_4(P^n, \dot{u}_z^n, \sigma_z^n) &= \frac{\nu R}{e} A_{I,J} \Delta z P_I^n + A_{I,J} E \Delta t (\theta - 1) \\
&\times [(\dot{u}_z)_{i+1}^n - (\dot{u}_z)_i^n] - A_{I,J} \Delta z (\sigma_z)_I^n.
\end{aligned} \tag{14b}$$

In the same manner, the lateral motion difference equations can be written as

$$\begin{aligned}
& \frac{A_f \Delta z}{\Delta t} (\dot{u}_y)_i^{n+1} + \frac{A_f}{\rho A} \theta [(\dot{Q}_y)_I^{n+1} - (\dot{Q}_y)_{I-1}^{n+1}] = f_5(\dot{u}_y^n, \dot{Q}_y^n), \\
& \frac{\theta}{\Delta z} [(\dot{u}_y)_{i+1}^{n+1} - (\dot{u}_y)_i^{n+1}] + \frac{1}{G A_t \Delta t} (Q_y)_I^{n+1} + \theta (\dot{\theta}_x)_I^{n+1} \\
& = f_6(\dot{u}_y^n, Q_y^n, \dot{\theta}_x^n), \\
& \frac{A_{I,J} \Delta z}{\Delta t} (\dot{\theta}_x)_i^{n+1} + \frac{A_{I,J}}{\rho I} \theta [(M_x)_I^{n+1} - (M_x)_{I-1}^{n+1}] \\
& - \frac{A_f \Delta z}{\rho I} \theta (Q_y)_i^{n+1} = f_7(Q_y^n, \dot{\theta}_x^n, M_x^n), \\
& \theta [(\dot{\theta}_x)_{i+1}^{n+1} - (\dot{\theta}_x)_i^{n+1}] + \frac{\Delta z}{E I_t \Delta t} (M_x)_I^{n+1} = f_8(\dot{\theta}_x^n, M_x^n).
\end{aligned} \tag{15a}$$

The related functions at one node at the n time layer can be written as

$$\begin{aligned}
f_5(\dot{u}_y^n, Q_y^n) &= \frac{A_f \Delta z}{\Delta t} (\dot{u}_y)_i^n + \frac{A_f}{\rho A} (\theta - 1) \\
&\times [(\dot{Q}_y)_I^n - (\dot{Q}_y)_{I-1}^n], \\
f_6(\dot{u}_y^n, Q_y^n, \dot{\theta}_x^n) &= \frac{\theta - 1}{\Delta z} [(\dot{u}_y)_{i+1}^n - (\dot{u}_y)_i^n]
\end{aligned}$$

$$\begin{aligned}
& + \frac{1}{G A_t \Delta t} (Q_y)_I^n + (\theta - 1) (\dot{\theta}_x)_I^n, \\
f_7(Q_y^n, \dot{\theta}_x^n, M_x^n) &= \frac{A_{I,J} \Delta z}{\Delta t} (\dot{\theta}_x)_i^n + \frac{A_f}{\rho I} (\theta - 1) \\
&\times [(\dot{M}_x)_I^n - (\dot{M}_x)_{I-1}^n] + \frac{A_f \Delta z}{\rho I} (1 - \theta) (Q_y)_I^n, \\
f_8(\dot{\theta}_x^n, M_x^n) &= (\theta - 1) [(\dot{\theta}_x)_{i+1}^n - (\dot{\theta}_x)_i^n] + \frac{\Delta z}{E I_t \Delta t} (M_x)_I^n.
\end{aligned} \tag{15b}$$

To solve the partial differential equations needs some conditions, called as solvability conditions. Usually, in region Ω ($x \in \Omega$), to satisfy the equation, the relationship of u at the boundary of region Ω is boundary condition.

The control equation system consists of the above eight partial differential equations. The conditions for constituting a well-posed problem are the initial conditions and the boundary conditions in different forms, which satisfy consistent, astringency and stability requirements. The initial conditions do not affect the solution, whereas most boundary conditions affect the form of discrete equations and the calculation method.

In the staggered grid, one-extra-layer nodes are set at the outside of the boundary, as shown in Fig. 4. Calculation is developed from the inner node ($I = 2$), the boundary node is used only for giving or calculating the boundary value.

(1) Physical boundary coincides with the control volume boundary.

(2) Nodes of outside layers are used to define, calculate or store the boundary values.

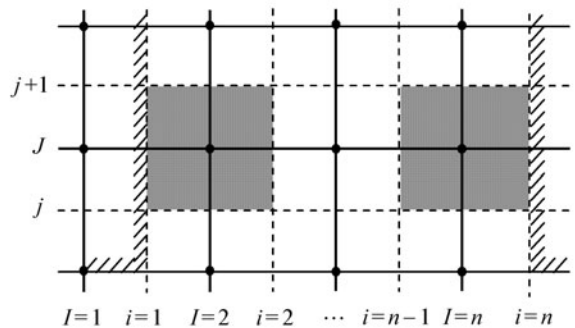


Fig. 4 Boundary grid configuration

These works minimize the changes of the discrete equations and the integral for the boundary of the control volume by the boundary condition.

The number of the physical and numerical boundaries at every boundary node is equal to the number of variables, to ensure the solution of these nodes. With consideration of the flow direction, the number of the physical boundary may be equal to the number of boundary node with input character. These two boundaries are shown in algebra form. If the number of the physical boundary is greater than that

for a well-posed problem, the extra ones are considered as additive boundary conditions.

The calculation form of the numerical boundary condition may be the same as the discrete form of the inner nodes. Due to the staggering of the discrete form of variables in the staggered grid system, the physical boundaries can be matched to the nodes of the control volume V , thus, the calculation form of the numerical boundaries is the same as the form of nodes of control volume P . The boundaries of the discrete form are self-contained when the number of physical quantities and the number of variables are equal.

4 Numerical example for testing

The experiment of University of Dundee is simulated by the method proposed in the present paper. The experimental apparatus consists of one long and one short stainless steel pipes screwed onto a rigid 90° elbow [3]. Inner diameter of the pipes is 52 mm, and the wall thickness is 3.9 mm. The pipes are filled with pressurized tap water (initial static pressure 2 MPa), with both ends closed. The pipes can move freely in a nearly horizontal plane because it is suspended on three long steel wires. Vibrations are generated by striking the closed end of the long pipe axially with a solid steel rod of 5 m length. Just before the impact, the rod moves with a constant velocity of 0.809 m/s.

The calculated and measured pressure results close to the elbow are shown in Fig. 5. The agreement between the numerical simulation of the FSI model by FVM and the experimental result is good. The results verified the rationality of the simulation of the FSI model by FVM, and the validity of the simulation code. These would facilitate further simulational studies.

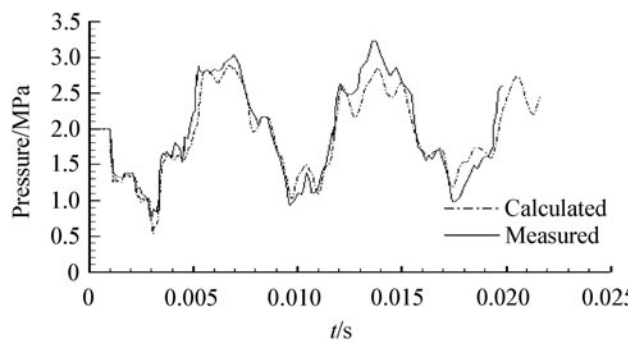


Fig. 5 Simulated and measured pressures close to the elbow

5 Numerical simulation of LOX feeding pipe before pump

For a typical launch vehicle, the FSI usually occurs in the

LOX feeding pipe systems. The system of LOX feeding pipe before pump is now analyzed. As shown in Fig. 6, the right Pipe 3 is the model of LOX feeding pipe. The middle Pipe 2 is the model whose two middle restrictions are absent. The left Pipe 1 is a straight pipe just for comparison, whose length is the same as the length of the other two pipes.

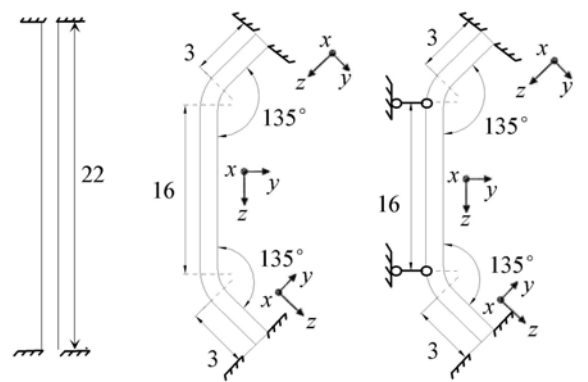


Fig. 6 Feeding Pipes 1, 2 and 3

The inlet of the pipes is also the outlet of the storage. The storage pressure at the outlet is $P_0 = 0.4$ MPa and the volume flux is $Q_0 = 0.2$ m³/s. The boundary conditions are

$$\begin{aligned} \dot{u}_z(0, t) &= 0, & P(0, t) &= P_0, \\ Q_y(0, t) &= 0, & M_x(0, t) &= 0. \end{aligned}$$

The end of the pipes is fixed. A spring pulse is set at the end, which is 1% flux reduction during 0.01 s. The flux oscillation is expressed as

$$\begin{aligned} Q(t) &= Q_0 - \frac{Q_0}{100}(1 - \tau), & \tau &= \left(1 - \frac{t}{t_c}\right)^{E_m}, \\ t_c &= 0.01 \text{ s}, & E_m &= 1.5. \end{aligned}$$

The initial stress, shearing force and bending moments are analyzed by the statics balance condition.

The pressure response to spring disturbance at the end of pipe is shown in Fig. 7.

For the straight Pipe 1, since the FSI effect is considered, in pressure response Curve 1 there appear many huckles oscillation compared with the traditional water hammer model. These huckles reflect the effect of the stress wave.

For Pipe 2, because of the junction coupling, the axial vibrations interact with the lateral vibrations, and thus Curve 2 becomes very complex. The spring pulse is applied in the axial direction, however, due to the axial and lateral balance, the vibration form is changed to the axial and lateral mixed vibration.

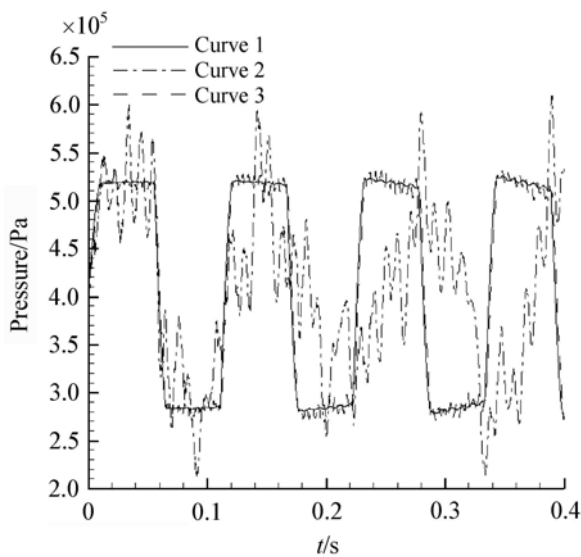


Fig. 7 Curves of the pressure response to spring disturbance at the end of pipe

For adding hinge bearings at the elbow as in Pipe 3, the effect of the interaction between the axial and lateral vibrations is reduced, which means less elbow junction coupling. The curve of Pipe 3 is similar to that of Pipe 1.

All power spectrum density estimates of these curves are shown in Figs. 8–10. The base frequency of Curve 1 is 9.26 Hz, and that of Curve 3 is 9.26 Hz, too. However, the base frequency of Curve 2 is 8.23 Hz, as shown in Fig. 9. Because the results of Curve 2 are affected by Poisson coupling and junction coupling, the pressure oscillation peak comes later than in other two curves. In addition, there are some high frequencies components in the power spectrum density estimate shown in Fig. 9, which reflect the effects of stress wave, shear wave and bending wave.

In addition, the power at the base frequency is also reduced for Curve 2. As the axial and lateral vibrations are

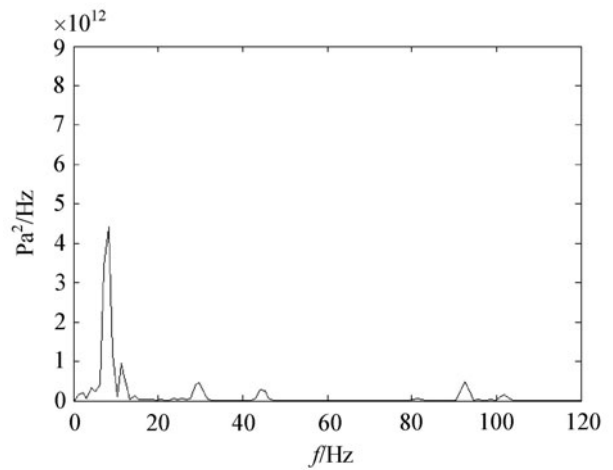


Fig. 9 Power spectrum density estimate of Curve 2

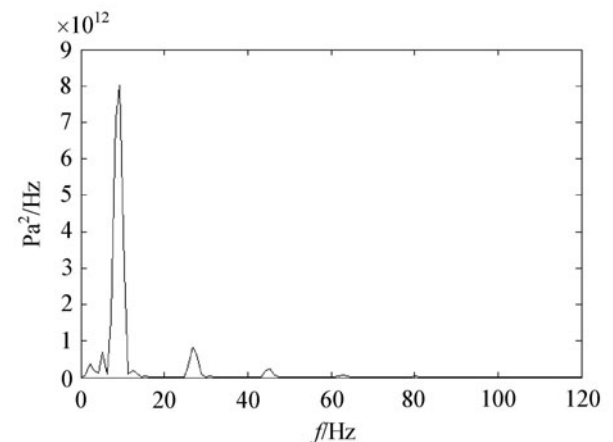


Fig. 10 Power spectrum density estimate of Curve 3

coupled, the amplitude power at the frequency of lateral vibration is increased, and thus that of axial low frequency vibration is reduced.

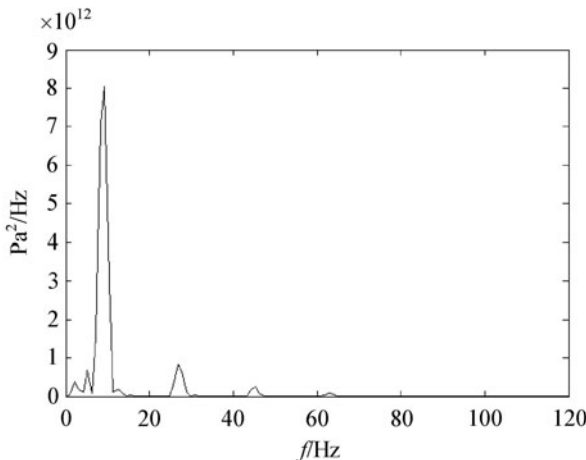


Fig. 8 Power spectrum density estimate of Curve 1

6 Summary

The simulation results of the FSI model by FVM are found in close agreement with the experiment results reported in literature, which validates the code of FVM. In the present simulation of LOX feeding pipe system, the axial and lateral vibrations are found to have severe interaction for the case without any restraint at the elbow. The simulation results show a complex pressure response curve resulting from the effect of elbow conjunction coupling. However, if the elbow vibration is restricted, the pressure response curve is similar to that of a straight pipe, due to the suppression effect of the elbow conjunction coupling. For complex feeding pipe systems used in space launch vehicles, if the dynamic

characteristics of pipes are to be analyzed accurately, the distribution of pipes, the elbow pipes and the restrictions are all needed to consider in detail.

References

- 1 Oppenheim, B.W., Rubin, S.: Advanced pogo stability analysis for liquid rockets. *Journal of Spacecraft and Rockets* **30**, 2048–2062 (1993)
- 2 Pilipenko, V.V.: Theoretical determination of amplitudes of longitudinal vibrations of liquid propellant launch vehicles. IAF-98-I.2.10 (1998)
- 3 Tijsseling, A.S., Vardy, A.E., Fan, D.: Fluid-structure interaction and cavitation in a single-elbow pipe system. *Journal of Fluids and Structures* **10**, 395–420 (1996)
- 4 Vardy, A.E., Fan, D., Tijsseling, A.S.: Fluid/structure interaction in a T-piece pipe. *Journal of Fluids and Structures* **10**, 763–786 (1996)
- 5 Skalak, R.: An extension of the theory of waterhammer. *Transactions of the ASME* **78**, 105–116 (1956)
- 6 Wiggert, D.C., Otwell, R.S., Hatfield, F.J.: The effect of elbow restraint on pressure transients. *ASME Journal of Fluids Engineering* **107**, 402–406 (1985)
- 7 Tijsseling, A.S.: Exact solution of linear hyperbolic four-equation system in axial liquid-pipe vibration. *Journal of Fluids and Structures* **18**, 179–196 (2003)
- 8 Zhang, X., Huang, S., Wang, Y.: The FEM of fluid structure interaction in piping pressure transients. In: Proceedings of the First International Conference on Flow Interaction, Hong Kong, September, 1994. 532–535 (1994)
- 9 Zhang, L.T., Gay, M.: Immersed finite element method for fluid-structure interactions. *Journal of Fluids and Structures* **23**, 839–857 (2007)
- 10 Giesecke, H.D.: Calculation of piping response to fluid transients including effects of fluid/structure interaction. In: *Transactions of SMiRT 6*, Paris, France, August 1981, Paper B 4/4 (1981)